Research Square

Preprints are preliminary reports that have not undergone peer review.
They should not be considered conclusive, used to inform clinical practice,
or referenced by the media as validated information.

Impact of Coupled Concentration-Field Physics on Molecular Dielectrophoresis

Reza Lotfi Navaei

University at Buffalo, State University of New York

Craig Snoeyink

craigsno@buffalo.edu

University at Buffalo, State University of New York

Article

Keywords: Dielectrophoresis, Microfluidics, Chemical-Potential-Transport

Posted Date: March 5th, 2026

DOI: https://doi.org/10.21203/rs.3.rs-8902824/v1

License: This work is licensed under a Creative Commons Attribution 4.0 International License.
Read Full License

Additional Declarations: No competing interests reported.

Impact of Coupled Concentration-Field Physics on Molecular Dielectrophoresis

Reza Lotfi Navaei[1] **and Craig Snoeyink**[1,*]

[1]Mechanical and Aerospace Engineering, University at Buffalo, 211 Bell Hall,Buffalo, 14260, NY, USA
[*]craigsno@buffalo.edu

ABSTRACT

Molecular dielectrophoresis is a microscale separation technique that is highly effective; however, there is a dearth of suitable models. This manuscript hypothesizes that incorporating positive feedback between local molecular concentration and local electric field strength will strengthen modeling efforts. The feedback effect occurs between the local electric field strength and the permittivity changes caused by variations in solute concentration but is challenging to integrate into conventional, force-based models of molecular dielectrophoretic transport. To address this gap, a continuum chemical transport model was constructed, and solute concentration transport was simulated in a simple microfluidic channel. By explicitly turning on and off the coupling between local electric field strength and local concentration, it was found that this coupling could be responsible for over a 20 fold increase in predicted solute concentration change. The magnitude of the synergistic increase in concentration changes is non-monotonic with both electric field gradient strength and average channel velocity, but is always strongly positive, suggesting that local electric field - concentration coupling is necessary for DEP modeling.

Keywords: Dielectrophoresis, Microfluidics, Chemical-Potential-Transport

Introduction

The molecular dielectrophoresis technique is an effective method for small-scale separation; nevertheless, it does not consist of a complete model[1,2]. Unlike conventional electrophoresis, which depends on the interaction between a net charge and a uniform electric field, dielectrophoresis (DEP) uses the interaction between an induced or permanent dipole and a spatially non-uniform electric field gradient to generate a translational force[3–5]. Although the fundamental physics of DEP have been well understood for several decades, the conventional mathematical approach has predominantly depended on the Clausius-Mossotti (CM) factor, an analytical approximation that considers particles as isolated point dipoles within a homogeneous medium[6–8]. From cell sorting to nanoparticle assembly, the CM factor has become the universal standard for quantifying polarizability in diverse dielectrophoretic studies[9–11].

For a spherical particle with radius r, the time-averaged dielectrophoretic force (DEP) is generally represented as:

$$\langle \mathbf{F}_{\mathrm{DEP}} \rangle = 2\pi \varepsilon_m \varepsilon_0 r^3 \mathrm{Re}[f_{\mathrm{CM}}] \nabla (E_{\mathrm{rms}})^2, \tag{1}$$

where,

$$f_{\mathrm{CM}} = \frac{\varepsilon_p^* - \varepsilon_m^*}{\varepsilon_p^* + 2\varepsilon_m^*}. \tag{2}$$

The gradient of the square of the root-mean-square electric field, $\nabla(E_{\mathrm{rms}})^2$, is proportional to the time-averaged dielectrophoretic (DEP) force, denoted as $\langle \mathbf{F}_{\mathrm{DEP}} \rangle$, which acts on a spherical particle of radius r. The dielectric properties of the system, specifically the vacuum permittivity ε_0 and the relative permittivity of the suspending medium ε_m, significantly influence the magnitude and direction of this force. The Clausius-Mossotti (CM) factor, f_{CM}, is a critical component of this relationship. It denotes the particle's effective polarizability in relation to its environment. The real part of this factor, $\mathrm{Re}[f_{\mathrm{CM}}]$, determines whether the particle is attracted to (positive DEP) or repelled from (negative DEP) regions of high electric field intensity. It is defined by the complex permittivities of the particle (ε_p^*) and the medium (ε_m^*). Nevertheless, as microfluidic applications advance towards higher concentrations of particles and more complex biological analytes, the limitations of this paradigm have become progressively evident[12,13].

While the Clausius-Mossotti approximation accurately predicts the dielectrophoretic behavior of micron-sized particles in linear regimes, its validity breaks down in microfluidic designs featuring high-gradient fields or nanoscale analytes[14]. The CM factor is based on the "isolated particle" approximation, which presumes that the particle is considerably smaller than the characteristic length scales associated with field non-uniformity[15]. Furthermore, conventional CM theory frequently proves insufficient for accurately representing experimental data of smaller biological entities like proteins[16]. This discrepancy arises because the theory neglects the molecular interactions between the analyte and the hydration shell of the surrounding medium. Consequently, the simplified dipole approximation often fails to capture the true dielectric behavior at the molecular scale[17]. The gap can be addressed by replacing discrete particle tracking with a continuum model that simulates the interaction between the electric field, the local species concentration (c), and the permittivity (ε)[18]. This enables simulation of high-density particle fronts and clusters that would otherwise be unresolvable[19].

Most current simulations employ a Lagrangian methodology, monitoring the trajectories of discrete, finite-sized particles through the application of Langevin or Stokesian dynamics equations[20,21]. Although effective for dilute suspensions, this approach becomes computationally infeasible as particle concentrations increase. Lagrangian models also generally neglect the "back-effect" whereby the existence of the particle influences the overall electric field. In contrast, the transport of species is addressed on a fixed spatial grid (Eulerian) rather than tracking individual positions. This approach is inherently more efficient for large-scale microfluidic designs and inherently incorporates multiple-body effects[22].

The existing literature typically considers the permittivity (ε_m) of the medium as a constant parameter[23,24]. However, in actual microfluidic systems, the local concentration of an analyte significantly impacts the effective permittivity of the suspension. Previous research has indicated that neglecting the feedback effects of ionic charge and concentration can result in errors in force computations[25–27]. Although certain "leaky dielectric"[28,29] or PNP (Poisson-Nernst-Planck)[30] models are available, they do not integrate the comprehensive thermodynamic coupling, in which the chemical potential is influenced by the electric field strength and vice versa[31,32]. This discrepancy can be resolved by shifting away from the CM-factor dipole approximation.

To address these gaps, this manuscript formulates transport equations derived from variations in the electrochemical potential. These equations account for the specific energy contributions of electric field-induced polarization in concentration-dependent media. Consequently, the model provides a complete coupling between the local electric field strength and the concentration of chemical species. The impact of this approach will be explored by simulating negative dielectrophoretic molecular transport of a solute within a channel flowing between two parallel-plate electrodes. By simulating this system in COMSOL, the electric field can be cleanly coupled or decoupled from the local concentration. This approach allows for a direct observation of how individual parameters influence the system's behavior. Consequently, the magnitude of these changes can be quantified and compared with high precision.

Methods

This study employs a numerical approach to investigate the transport behavior of molecules under dielectrophoretic forces. A continuum modeling framework was developed to simulate the DEP transport equation, coupled with fluid flow and electric field distribution.

Continuum Transport Model

To analyze the system, numerical simulations were developed to resolve the coupling between hydrodynamics, electrostatics, and particle transport. These simulations allow the electric field to be isolated from, or coupled to, the local species concentration. As a result, the specific magnitude of the observed physical changes can be accurately quantified. The particle transport was modeled using a generalized flux equation influenced by gradients in the chemical potential. The temporal evolution of the concentration of solutes c is governed by the convection diffusion equation[33]:

$$\frac{\partial c}{\partial t} = \nabla \cdot \left(c \frac{D}{RT} \nabla \mu - \mathbf{v} c \right) \tag{3}$$

Where c is the solute concentration, D is the diffusion coefficient, R is the universal gas constant, T is the absolute temperature, $\mathbf{v}$ is the fluid velocity vector (advection) and μ is the total chemical potential of the solute.

The chemical potential μ indicates the thermodynamic drive for molecular transport. This system is characterized as the combined effect of the chemical potential of an ideal solution (entropy of mixing) and the potential energy contribution from the external electric field (dielectrophoretic contribution):

$$\mu = \mu_0 + RT \ln(c) + \mu_{DEP} \tag{4}$$

where μ_0 is the standard chemical potential, $RT\ln(c)$ represents the entropic term driving diffusion, and μ_{DEP} is the chemical potential associated with the dielectrophoretic force[34].

The chemical potential of DEP μ_{DEP} is associated with the intensity of the local electric field and is defined as:

$$\mu_{DEP} = \frac{1}{2}\varepsilon_0 E^2 \frac{\partial \varepsilon}{\partial c} \tag{5}$$

Where ε_0 is the vacuum permittivity, E is the electric field norm, and $\frac{\partial \varepsilon}{\partial c}$ represents the variation of the permittivity of the solution with respect to the concentration of the solute.

Substituting the definitions of chemical potential and the DEP energy term back into the governing equation yields the final expanded transport equation solved in this study:

$$\frac{\partial c}{\partial t} = \nabla \cdot \left(D\nabla c + \frac{Dc}{2RT}\varepsilon_0 \nabla \left(E^2 \frac{\partial \varepsilon_r}{\partial c} \right) - \mathbf{v}c \right) \tag{6}$$

To accurately calculate the thermodynamic force term ($\frac{\partial \varepsilon}{\partial c}$), the relative dielectric permittivity of the solution, $\varepsilon_{\mathrm{sol}}(\mathrm{c})$, was modeled as a nonlinear function of the molecule concentration. For this study the following dielectric constant function for $NiCl_2$ was used[35]:

$$\varepsilon_{sol}(c) = 78.36 - 25c + 8.7c^2. \tag{7}$$

Equation 7 explains the variation in the effective polarizability of the medium as the local concentration of the solute changes. This explicitly links the electric field distribution to the solute concentration and the transport equation when the electric field is solved using this solution permittivity.

The computational model was implemented using *COMSOL Multiphysics* 6.3 to solve the coupled equations within a 2D domain that represents the geometry of the microfluidic channel. The simulation incorporated the *Electrostatics* interface (resolving the Laplace equation, $\nabla^2\phi = 0$) and the *Laminar Flow* interface (addressing the Navier-Stokes equations) alongside the *General Form of PDE* interface to model the revised transport equation. Boundary conditions were established to accurately reflect the experimental configuration: no-slip conditions were imposed on all channel walls for fluid flow, while no-flux insulation conditions were applied to molecule concentration at the boundaries.

To determine the impact of fully coupling fields and transport, a simple 2D microfluidic system was created as shown in Figure 1. A uniform channel with uniform height h is passed between two electrodes of width $w_{electrode}$ where $w_{electrode} >> h$. The channel contains a mixture of water/$NiCl_2$ with permittivity given by the equation 7 and a viscosity of 0.98 mPa.s[36]. The potential of the two electrodes is maintained at a set voltage (V) and the concentration map is obtained after allowing the system to reach a steady state.

Mesh Independence Study

A detailed study of the mesh independency was conducted using the Grid Convergence Index (GCI) method to ensure numerical precision and to verify that the solution was independent of spatial discretization[37]. Ten distinct mesh sizes have been evaluated, ranging from coarse to extremely fine resolutions. The GCI offers a standardized metric for convergence and assesses the discretization error. The process involved determining the representative grid size (Δx) and the refinement ratio $r = \Delta x_{coarse}/\Delta x_{fine}$. The convergence order (p) was computed iteratively utilizing the solutions from three successive grids ($\mathrm{f}_1, \mathrm{f}_2, \mathrm{f}_3$), and the Grid Convergence Index (GCI) was established using the following expression:

$$GCI_{fine} = \frac{F_s|\varepsilon|}{r^p - 1} \tag{8}$$

Where F_s is the safety factor (set to 1.25 for three grids or more) and ε is the relative error between the fine and medium grids defined as: $(f_3 - f_2)/f_3$.

The analysis demonstrated in Figure 2 showed monotonic convergence throughout the enhanced meshes. The plot and the calculated GCI values show that the mesh comprising 620,400 elements produced a GCI of approximately 0.57%, suggesting that additional refinement would lead to minimal changes in the solution (<1%). Thus, the 620,400-element mesh was chosen for all subsequent simulations as it offered the ideal equilibrium between computational efficiency and numerical precision.

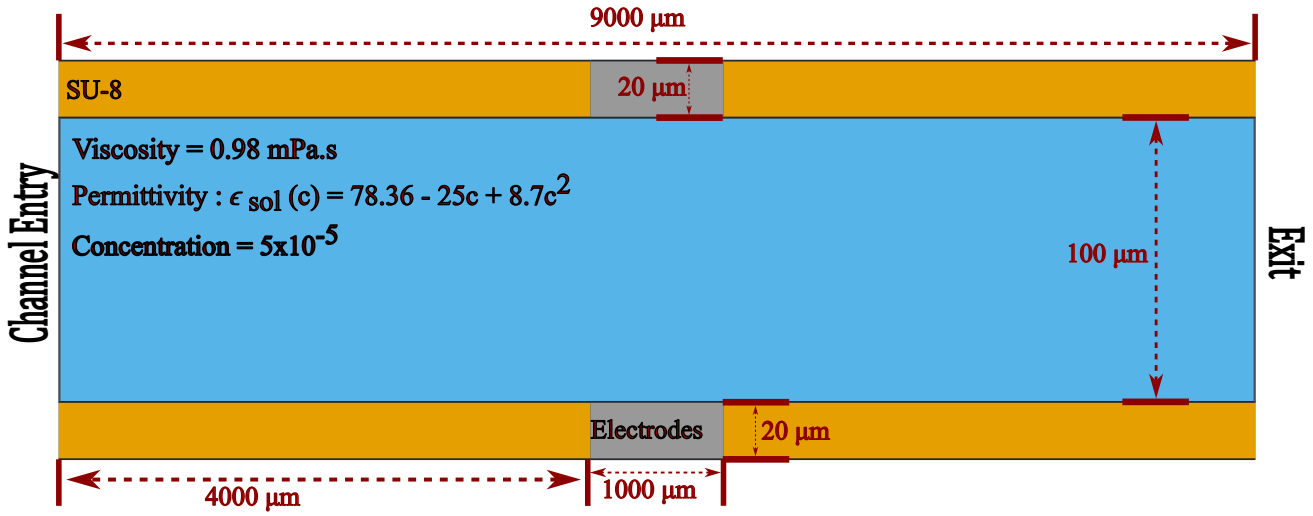


Figure 1. Schematic layout and boundary conditions of the microfluidic device. The channel features a total length of 9000 μm and a width of 100 μm, with 20 μm thick SU-8 insulating walls. A pair of 1000 μm long electrodes are positioned 4000 μm from the channel entry to facilitate the dielectrophoretic force. The working fluid properties are defined by a dynamic viscosity of 0.98 mPa $\cdot$ s and a concentration-dependent relative permittivity (ε_{sol}) as shown in the entry region.

Table 1. GCI values and grid sizes.

f_3 (fine)	f_2	f_1 (coarse)	Coarse to Medium (%)	Medium to Fine (%)
13951547	9795593	6292018	0.00013	0.00001
9795593	6292018	1640734	0.03733	0.03330
6292018	1640734	1348943	0.01664	0.00833
1640734	1348943	955691	0.02720	0.02970
1348943	955691	620400	0.16059	0.11972
955691	620400	365735	0.26049	0.16753
620400	365735	175344	0.60785	0.56621

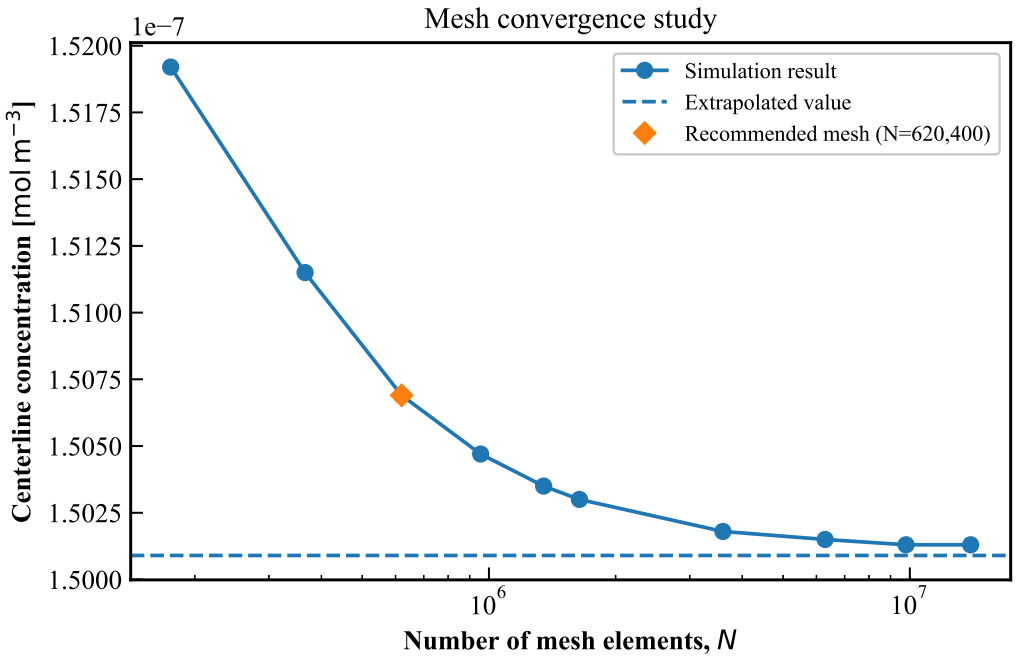


Figure 2. Mesh Convergence Plot comparing the accumulated Concentration in the centerline of the channel vs. Number of mesh Elements.

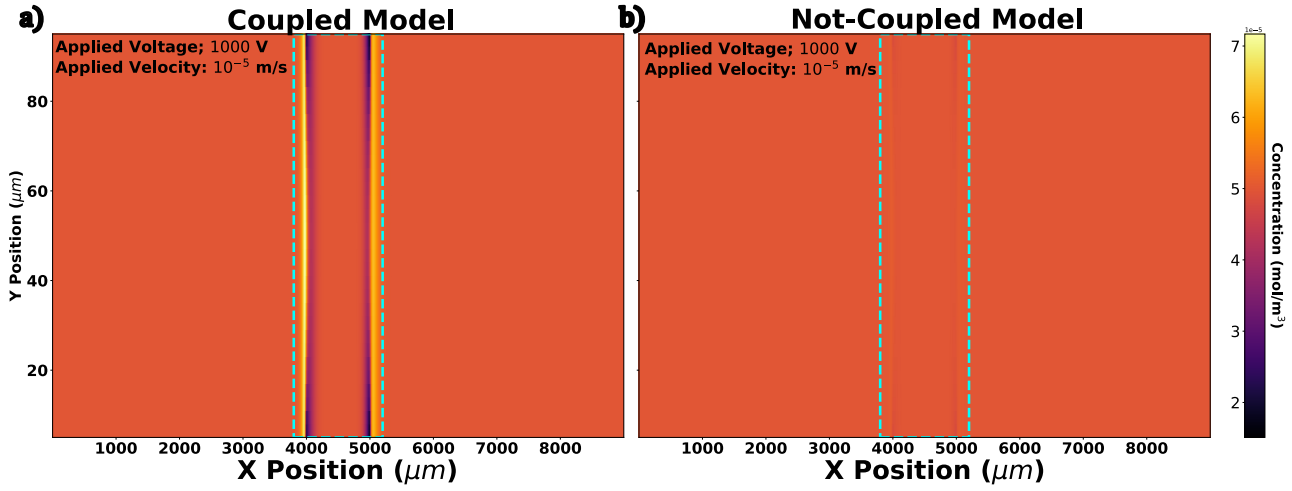


Figure 3. Example map of steady-state of solute concentration within the channel with both, a)coupled and, b) uncoupled physics. Both simulations utilized an electrode potential of 1000 V, an average velocity of 5.0×10^{-5} M, initial solute concentration of 5.0×10^{-5} M, and a channel width of 100 μm. The solute has a negative dielectric decrement and so experiences negative dielectrophoresis and builds in concentration before and after the electric field. Note that the coupled physics simulation shows a nearly 2000% higher change in concentration.

Results

Figure 3 shows an example of the simulated steady-state concentration maps with both a) fully-coupled and b) uncoupled field-concentration physics. All other simulation parameters are kept the same: the electrode potential is 1000 V, the mean velocity of the solution is 1.0×10^{-5}m/s, the initial and input concentrations are 5.0×10^{-5} M, and the electrode spacing (h) is 100 μm. As expected, large changes in concentration occur near the entrance and exit of the electrode region, where the electric field gradient is highest. The concentration profile along the channel axis will be explored in more detail later but it is notable that the concentration variations for the fully coupled physics simulation are much larger than the uncoupled version, over 2000% larger in magnitude.

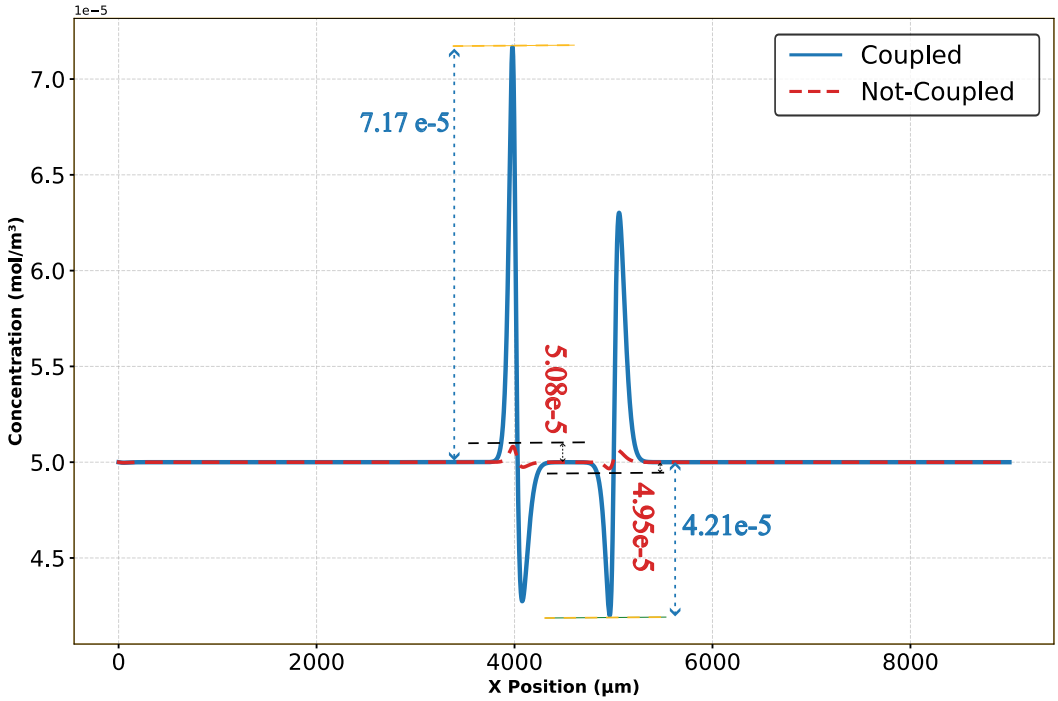


Figure 4. Plot of concentration magnitude along channel axis for coupled (blue) and uncoupled (red) physics simulations. The change in concentration is 2277% higher for the coupled physics as a result of the increase in electric field gradient brought on by the change in concentration dependent permittivity.

The magnitude of this difference is more obvious in the concentration plots along the channel axis shown in Figure 4 for both coupled (solid blue) and uncoupled (dashed red) simulations. The negative dielectric decrement of the water/$NiCl_2$ solution results in negative dielectrophoresis, resulting in the solute concentration before the electrode region building to 7.17×10^{-5} M for the coupled simulation and 5.08×10^{-5} M for the uncoupled simulation. This is a remarkable 2277% increase, indicating that fully coupling the local electric field to the local concentration results in much stronger dielectrophoretic transport.

The reason for this significant increase in DEP transport can be seen in Figure 5 where the magnitude of the magnitude of the electric field is plotted squarely for both coupled and uncoupled simulations. As can be seen in this plot, variations in concentration create local variations in electric field strength that enhance the electric field gradients, increasing dielectrophoretic transport and synergistically magnifying the variations in concentration. In this particular case, the square of the electric field gradient increases by 7%.

Geometric Scaling and Gradient Isolation

To further explore the relationship between electric field gradients and the impact of coupling the local electric field to concentration, electrode spacing (h) and electrode potential (V) were simultaneously varied to maintain the nominal external electric field (calculated as $E_{nom} = V/h$) while varying the magnitude of the electric field gradient. By simultaneously halving the channel width (h) and the applied voltage (V), the magnitude of the general electric field ($E \approx V/h$) remains unchanged; while the field gradient ∇E^2 is substantially amplified.

In order to quantify the impact of the field-concentration coupling effect on solute transport, we introduced a dimensionless metric known as the Coupling Enhancement Ratio (η). This metric measures the percentage change between the normalized

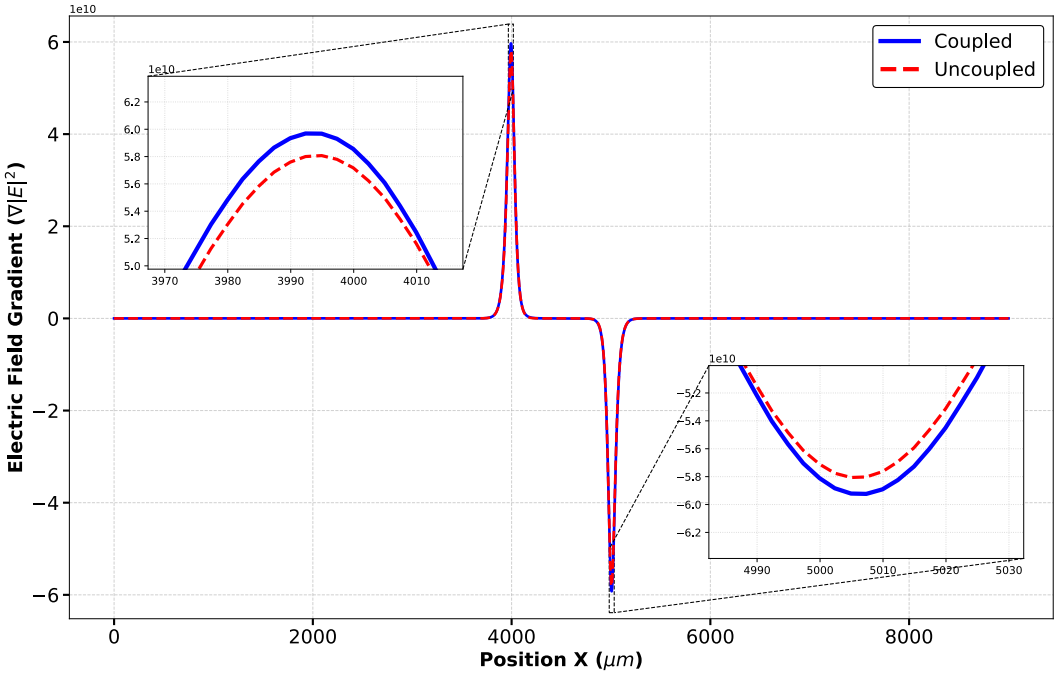


Figure 5. Plot of electric field gradient ($\nabla|E|^2$) profile along the microchannel for an initial solution concentration (c_{in}) of 10^{-3}, comparing the coupled (solid blue) and uncoupled (dashed red) numerical approaches. The zoomed areas show the local enhancement of the field gradient at the electrode boundaries, demonstrating that coupling of the local electric field to the local concentration increases the electric field gradients.

concentration variance of the coupled model to the uncoupled baseline. Initially, a normalized response ratio (R) is determined for both the coupled (R_c) and uncoupled (R_{nc}) cases. This ratio is defined as the peak-to-peak concentration difference in relation to the initial background concentration (C_0). The Coupling Enhancement Ratio is subsequently defined as the percentage increase in this response ratio relative to the uncoupled case given as:

$$\begin{aligned} R_c &= \frac{\max(C_{coupled}) - \min(C_{coupled})}{C_0} \\ R_{nc} &= \frac{\max(C_{uncoupled}) - \min(C_{uncoupled})}{C_0} \\ \eta &= \left(\frac{R_c - R_{nc}}{R_{nc}}\right) \times 100 \end{aligned} \tag{9}$$

The results, shown in Table 2, show that while E is constant, the impact of field-concentration coupling (measured as the Ratio of changes in concentration) changes nonlinearly with the reduced channel width. The ratio of concentration changes

Table 2. Scaling factor comparison for coupled and not-coupled cases.

Scaling Factor	Coupled ($\times 10^{-5} M$)		Not-Coupled ($\times 10^{-5} M$)		Ratio (%)
	Max	Min	Max	Min	
4	5.30	4.85	5.03	5.00	1500
2	6.01	4.62	5.06	4.99	1986
1	7.17	4.21	5.08	4.95	2277
0.5	8.90	3.57	6.97	4.08	184
0.25	10.60	2.11	8.12	3.33	177

initially increases with decreasing channel width, and then subsequently decreases. This non-linear behavior is a result of the non-linear nature of the solution permittivity curve given by Equation 7. As the concentration increases, slope of the curve decreases, (i.e. the dielectric decrement magnitude becomes smaller with increasing concentration). Marginal increases in concentration have less of an impact on local electric field strength, and the effect of coupled physics decreases relative to the uncoupled state.

Influence of Initial Species Concentration

To further explore the effect of non-linear solution permittivity on the coupled-physics impact, this subsection examines the influence of the initial concentration c_{in} of the analyte on transport dynamics across twenty distinct concentration levels given in Table 3. Four different metrics were explored, the results of which are shown in Figure 6. Figure 6a shows how the response ratio for coupled (solid blue) and uncoupled (dashed red) behaves while Figure 6b combines these two metrics to show enhancement ratio. Finally, Figures 6c and d show the changes in electric field gradient and electric field norm, respectively.

In all metrics, the effects of non-linear solution permittivity begin to become significant only at concentrations larger than 5×10^{-2} mol/m^3, at which point both the response ratio (Figure 6a) and the enhancement ratio (Figure 6b) both start to decrease. Figures 6c and 6d both show that the effect of coupling physics on the electric field begins at much smaller concentrations, but it is not until the much higher concentration of 5×10^{-2} mol/m^3 that the non-linear nature of the solution permittivity begins to saturate the effect. Additionally, the impact of couple physics is maintained even at very low concentrations, where changes in electric field magnitude and gradient might be minimal.

Table 3. Initial concentrations (M)

1.00×10^{-5}	3.26×10^{-4}	3.16×10^{-3}	2.52×10^{-2}
2.46×10^{-5}	4.04×10^{-4}	5.00×10^{-3}	4.00×10^{-2}
5.00×10^{-5}	5.93×10^{-4}	7.47×10^{-3}	5.97×10^{-2}
9.20×10^{-5}	9.43×10^{-4}	9.04×10^{-3}	8.50×10^{-2}
1.26×10^{-4}	1.83×10^{-3}	1.06×10^{-2}	1.00×10^{-1}

Impact of Convection and Applied Voltage

Convective transport and applied voltage are both experimental parameters that can easily be altered and so it is an important question as to how these parameters alter the impact of the physics coupling. Increasing the applied voltage increases DEP transport, and which presumably increases the synergistic concentration enhancement. Convective transport opposes DEP and is therefore expected to do the opposite. Our parametric study of the concentration enhancement ratio shows that this is largely the case with one interesting exception.

Figure 7 shows the results of the parametric study that simultaneously varies the voltage and average channel velocity. As expected, maintaining the flow velocity constant and increasing the applied voltage result in an increase in concentration enhancement. Increasing voltage activates the synergistic relationship between concentration gradients and DEP, further increasing the concentration of the solute at the leading edge of the electrodes.

In contrast, the effect of increasing flow velocity is non-monotonic. Increasing flow velocity initially reinforces the physics-coupling induced concentration enhancement. Further increasing the flow velocity while holding velocity constant will eventually result in a decrease of concentration enhancement showing that while the impact of physics-coupling might be more robust to convection, eventually convection becomes strong enough to negatively impact the synergistic relationship between concentration gradients and DEP transport, decreasing the overall concentration enhancement.

Discussion

The results presented here show that even at very low concentrations, the synergistic coupling between local electric field strengths and local concentration is an essential component of molecular DEP transport modeling. This synergistic relationship, where DEP induced concentration gradients induce electric field gradients that further enhance concentration gradients, increases in strength with increasing applied voltage and decreases at large concentrations as the concentration-permittivity relationship saturates.

However, the magnitude of this synergistic feedback loop is a non-monotonic function of both flow velocity and the square of the electric field gradient. In both cases, while the coupled and un-coupled physics models show different sensitivity to these parameters, the coupled physics model always shows a stronger increase in concentration.

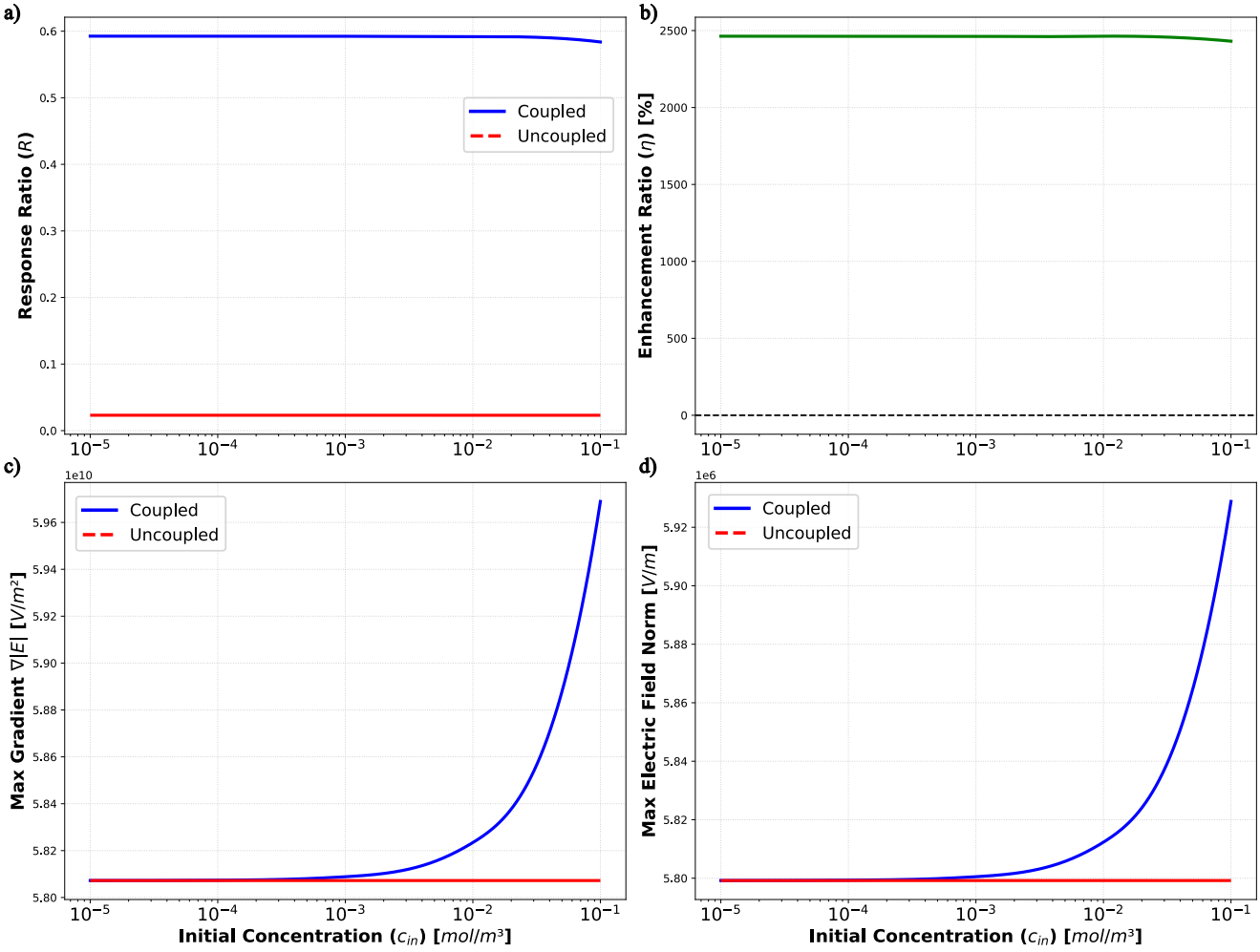


Figure 6. Comparative analysis of transport metrics as a function of initial concentration (c_{in}). a) Response Ratio (R) indicating focusing intensity. b) Coupling Enhancement Ratio (η) showing the percentage gain attributed to concentration effects. c) Maximum gradient of the electric field norm ($\nabla|E|$). d) Maximum electric field norm ($|E|$).

Table 4. Voltages and flow velocities used in the study.

Voltages (V)				Flow velocities (m/s)	
0	630	800	910	1.00×10^{-5}	1.79×10^{-4}
200	670	825	930	1.14×10^{-5}	3.03×10^{-4}
425	705	850	970	2.09×10^{-5}	4.75×10^{-4}
510	740	870	985	4.67×10^{-5}	7.05×10^{-4}
575	770	890	1000	9.69×10^{-5}	1.00×10^{-3}

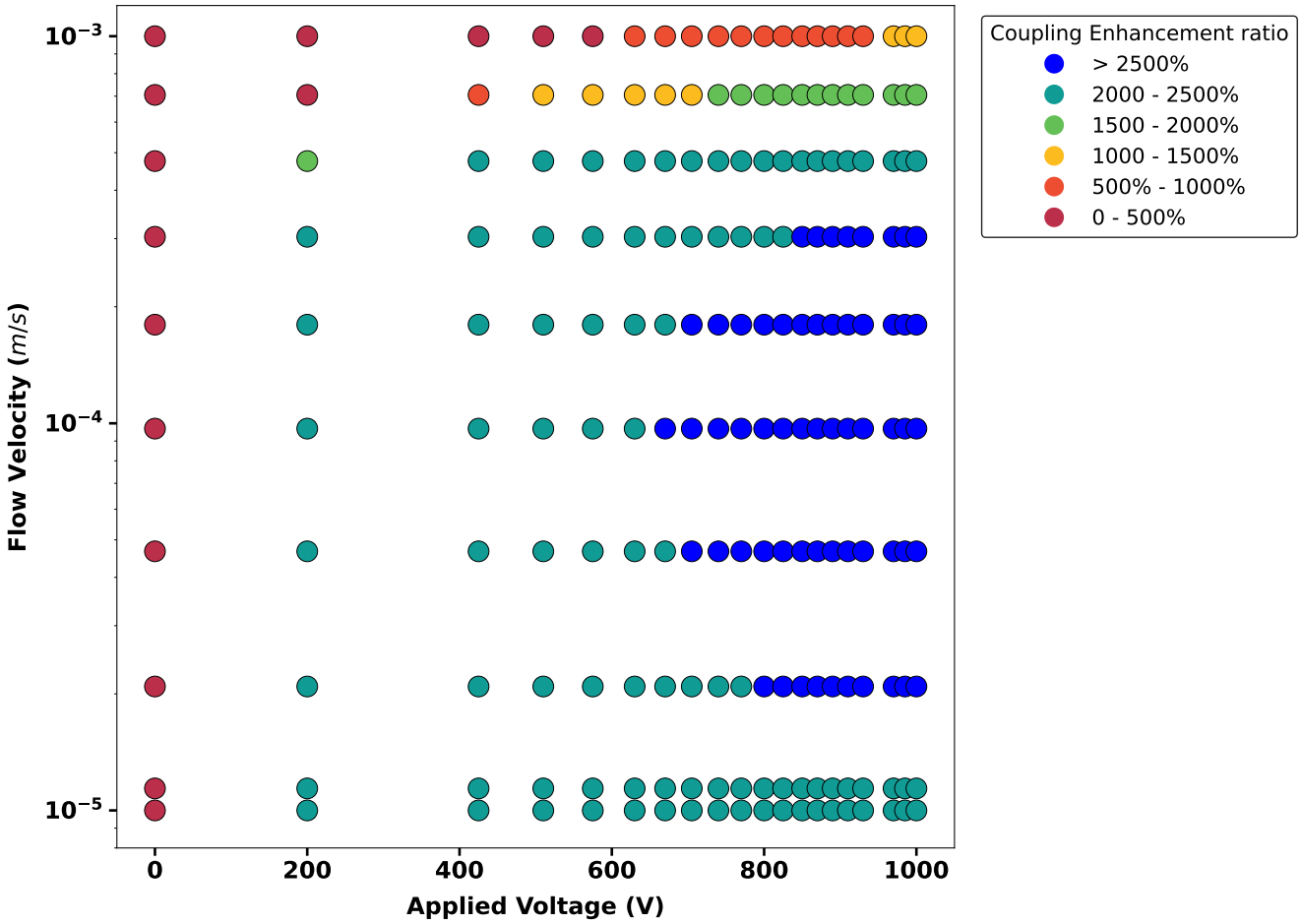


Figure 7. Plot of parametric phase map of coupling enhancement. Discrete data points indicate the coupling enhancement ratio across a logarithmic scale of flow velocities (10^{-5} to 10^{-3} m/s) and linearly scaled voltages up to 1000 V. The color transition from blue to red signifies an increase in the enhancement ratio from 34% to over 2500%.

Collectively, these results highlight the critical necessity of including the coupling between the local electric field and species concentration. This synergistic interaction is fundamental to accurately capturing molecular transport behavior. Therefore, future modeling efforts must incorporate these coupled fluid-field physics to ensure high-fidelity predictions. Historically, models of molecular dielectrophoresis have underestimated the norm of the DEP force by orders of magnitude. The magnitude of the concentration enhancement shown here, between 34% and 2500%, is of the order of magnitude to bring these models into much closer alignment with experimental results.

References

1. Gascoyne, P. R. C. & Vykoukal, J. Particle separation by dielectrophoresis. *Electrophoresis* **23**, 1973, DOI: 10.1002/1522-2683(200207)23:13<1973::AID-ELPS1973>3.0.CO;2-1 (2026-01-13).

2. Nguyen, T. H. *et al.* Numerical study on a facing electrode configuration dielectrophoresis microfluidic system for efficient biological cell separation. *Sci. Reports* **14**, 27627, DOI: 10.1038/s41598-024-78722-7 (2024-11-11).

3. Abd Rahman, N., Ibrahim, F. & Yafouz, B. Dielectrophoresis for biomedical sciences applications: A review. *Sensors* **17**, 449, DOI: 10.3390/s17030449 (2017-02-24).

4. Hadjiaghaie Vafaie, R., Poorreza, E., Sheykhivand, S. & Danishvar, S. A bionic sensing platform for cell separation: Simulation of a dielectrophoretic microfluidic device that leverages dielectric fingerprints. *Biomimetics* **10**, 753, DOI: 10.3390/biomimetics10110753 (2025).

5. Zavatski, S., Bandarenka, H. & Martin, O. J. F. Protein dielectrophoresis with gradient array of conductive electrodes sheds new light on empirical theory. *Anal. Chem.* **95**, 2958–2966, DOI: 10.1021/acs.analchem.2c04708 (2023-02-07).

6. Pethig, R. The clausius–mossotti factor in dielectrophoresis: A critical appraisal of its proposed role as an 'electrophysiology rosetta stone'. *Micromachines* **17**, 96, DOI: 10.3390/mi17010096 (2026).

7. Hu, S., Ji, J., Chen, X. & Tong, R. Dielectrophoresis: Measurement technologies and auxiliary sensing applications. *Electrophoresis* **45**, 1574–1596, DOI: 10.1002/elps.202300299 (2024-09).

8. O'Donnell, M. C., Kepper, M. & Pesch, G. R. A brief history and future directions of dielectrophoretic filtration: A review. *Electrophoresis* **46**, 1112–1132, DOI: 10.1002/elps.202400116 (2025-08).

9. Yao, J., Zhao, K., Lou, J. & Zhang, K. Recent advances in dielectrophoretic manipulation and separation of microparticles and biological cells. *Biosensors* **14**, 417, DOI: 10.3390/bios14090417 (2024-08-27).

10. Pesch, G. R. & Du, F. A review of dielectrophoretic separation and classification of non-biological particles. *Electrophoresis* **42**, 134–152, DOI: 10.1002/elps.202000137 (2021-01).

11. Yu, C.-X., Chang, C.-C., Huang, K.-H. & Fu, L.-M. Electrokinetic microfluidics at the convergence frontier: From charge-driven transport to intelligent chemical systems. *Micromachines* **17**, 71, DOI: 10.3390/mi17010071 (2025-12-31).

12. Yan, Y., Luo, J., Guo, D. & Wen, S. Dynamic dielectrophoresis model of multi-phase ionic fluids. *PLOS ONE* **10**, e0117456, DOI: 10.1371/journal.pone.0117456 (2015-02-20). Publisher: Public Library of Science.

13. Zulfiqar, M. *et al.* Experimental study on multi-cell counting using an inertial microfluidic device. *Appl. Sci.* **15**, 5701, DOI: 10.3390/app15105701 (2025).

14. Shee, Z. D. E., Mhd Noor, E. E. & Baig, M. F. Protein manipulation via dielectrophoresis: Theoretical principles and emerging microfluidic platforms. *Micromachines* **16**, 531, DOI: 10.3390/mi16050531 (2025-04-29). Publisher: MDPI AG.

15. Camarda, M. *et al.* Theoretical and experimental study of the role of cell-cell dipole interaction in dielectrophoretic devices: application to polynomial electrodes. *BioMedical Eng. OnLine* **13**, 71, DOI: 10.1186/1475-925X-13-71 (2014).

16. Pethig, R. Protein dielectrophoresis: A tale of two clausius-mossottis—or something else? *Micromachines* **13**, DOI: 10.3390/mi13020261 (2022).

17. Seyedi, S. S. & Matyushov, D. V. Protein dielectrophoresis in solution. *The J. Phys. Chem. B* **122**, 9119–9127, DOI: 10.1021/acs.jpcb.8b06864 (2018-10-04). Publisher: American Chemical Society.

18. Giesler, J., Weirauch, L., Thöming, J. & Baune, M. Compensation of capacitive currents in high-throughput dielectrophoretic separators. *Sci. Reports* **14**, 16491, DOI: 10.1038/s41598-024-67030-9 (2024-07-17).

19. Yang, J., Christov, I. C. & Dong, S. Phase field modeling and numerical algorithm for two-phase dielectric fluid flows. *J. Comput. Phys.* **514**, 113228, DOI: 10.1016/j.jcp.2024.113228 (2024-10-01).

20. Lee, Y. J., Jin, H., Kim, D. Y., Kang, S. & Ahn, K. H. Lagrangian-based simulation method using constrained stokesian dynamics for particulate flows in microchannel. *J. Fluid Mech.* **990**, A3, DOI: 10.1017/jfm.2024.493 (2024). Edition: 2024/08/12 Publisher: Cambridge University Press.

21. Michael, A. J., Mark, A., Sasic, S. & Ström, H. A nonlocal multiscale model for brownian particles: Application to hindered deposition in microfluidic systems. *Int. J. Multiph. Flow* **193**, 105421, DOI: 10.1016/j.ijmultiphaseflow.2025.105421 (2025-12-01).

22. Chen, C.-H. & Yaji, K. Topology optimization for microchannel heat sinks with nanofluids using an eulerian-eulerian approach. *Int. J. Heat Mass Transf.* **243**, 126870, DOI: 10.1016/j.ijheatmasstransfer.2025.126870 (2025-06-15).

23. Mondal, B. & Bhattacharyya, S. Effects of electrostatic correlations and ion–solvent interactions of finite-sized ions on the electrophoresis of a soft particle. *J. Fluid Mech.* **1006**, A9, DOI: 10.1017/jfm.2025.17 (2025-03-10).

24. Dorfman, K. D., King, S. B., Olson, D. W., Thomas, J. D. P. & Tree, D. R. Beyond gel electrophoresis: Microfluidic separations, fluorescence burst analysis, and DNA stretching. *Chem. Rev.* **113**, 2584–2667, DOI: 10.1021/cr3002142 (2013-04-10). Publisher: American Chemical Society.

25. Delgado, A., González-Caballero, F., Hunter, R., Koopal, L. & Lyklema, J. Measurement and interpretation of electrokinetic phenomena. *Elkin 06, Int. Electrokinet. Conf. June 25-29, Nancy, France* **309**, 194–224, DOI: 10.1016/j.jcis.2006.12.075 (2007-05-15).

26. Bazant, M. Z. & Squires, T. M. Induced-charge electrokinetic phenomena. *Curr. Opin. Colloid & Interface Sci.* **15**, 203–213, DOI: 10.1016/j.cocis.2010.01.003 (2010-06-01).

27. Bazant, M. Z., Sabri Kilic, M., Storey, B. D. & Ajdari, A. Nonlinear electrokinetics at large voltages. *New J. Phys.* **11**, 075016, DOI: 10.1088/1367-2630/11/7/075016 (2009-07-31).

28. Schnitzer, O. & Yariv, E. The taylor–melcher leaky dielectric model as a macroscale electrokinetic description. *J. Fluid Mech.* **773**, 1–33, DOI: 10.1017/jfm.2015.242 (2015). Edition: 2015/05/14 Publisher: Cambridge University Press.

29. Mori, Y. & Young, Y.-N. From electrodiffusion theory to the electrohydrodynamics of leaky dielectrics through the weak electrolyte limit. *J. Fluid Mech.* **855**, 67–130, DOI: 10.1017/jfm.2018.567 (2018). Edition: 2018/09/14 Publisher: Cambridge University Press.

30. Zheng, Q. & Wei, G.-W. Poisson–boltzmann–nernst–planck model. *The J. Chem. Phys.* **134**, 194101, DOI: 10.1063/1.3581031 (2011-05-21).

31. Pethig, R. Limitations of the clausius-mossotti function used in dielectrophoresis and electrical impedance studies of biomacromolecules. *Electrophoresis* **40**, 2575–2583, DOI: 10.1002/elps.201900057 (2019-09).

32. Liu, J.-L. & Eisenberg, B. Molecular mean-field theory of ionic solutions: A poisson-nernst-planck-bikerman model. *Entropy* **22**, 550, DOI: 10.3390/e22050550 (2020).

33. Zhu, J. & Xuan, X. Dielectrophoretic focusing of particles in a microchannel constriction using DC-biased AC flectric fields. *Electrophoresis* **30**, 2668–2675, DOI: 10.1002/elps.200900017 (2009-08).

34. Alberty, R. A. USE OF LEGENDRE TRANSFORMS IN CHEMICAL THERMODYNAMICS. *Pure Appl. Chem.* 32 (2001).

35. Collie, C. H., Hasted, J. B. & Ritson, D. M. The dielectric properties of water and heavy water. *Proc. Phys. Soc.* **60**, 145–160, DOI: 10.1088/0959-5309/60/2/304 (1948-02-01).

36. Afzal, M., Saleem, M. & Mahmood, M. T. Temperature and concentration dependence of viscosity of aqueous electrolytes from 20.degree.c to 50.degree.c chlorides of (sodium(1+), potassium(1+), magnesium(2+), calcium(2+), barium(2+), strontium(2+), cobalt(2+), nickel(2+), copper(2+) and chromium(3+). *J. Chem. & Eng. Data* **34**, 339–346, DOI: 10.1021/je00057a023 (1989-07).

37. Roache, P. J. Perspective: A method for uniform reporting of grid refinement studies. *J. Fluids Eng.* **116**, 405–413, DOI: 10.1115/1.2910291 (1994-09-01).

Acknowledgements

The authors express their sincere gratitude to Sarah Hamdan, Sampada Mahesh Khanvilkar, and Arjun Patel for their valuable insights and assistance in reviewing the manuscript.

Funding

This material is based on work supported by the U.S. Department of Energy, Office of Science, Office of Basic Energy Sciences, under Award Number DE-SC0025463.

Author contributions statement

RLN: Conceptualization, Methodology, Software, Validation, Formal analysis, Investigation, Data curation, Writing- original draft. CS: Conceptualization, Methodology, Formal analysis, Supervision, Project administration, Funding acquisition, Writing – review and editing. Both authors contributed to the post-processing of the data and the preparation of the final manuscript.

Data availability

All analytical data is provided within the request of reviewers and readers.

Competing Interests

The authors declare no competing interests.